

pubs.acs.org/cm Article

Thermal Stability of Quasi-1D NbS₃ Nanoribbons and Their Transformation to 2D NbS₂: Insights from *in Situ* Electron Microscopy and Spectroscopy

Eric V. Formo,* Jordan A. Hachtel, Yassamin Ghafouri, Matthew A. Bloodgood, and Tina T. Salguero*



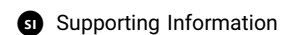
Cite This: Chem. Mater. 2022, 34, 279-287



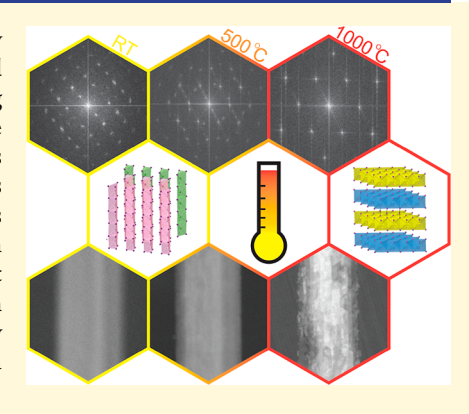
ACCESS I

Metrics & More





ABSTRACT: In situ electron microscopy imaging and spectroscopy enabled us to study the evolution of quasi-1D NbS₃-IV nanoribbons with respect to morphology and chemical structure at temperatures between room temperature and 1000 °C. Scanning transmission electron microscopy (STEM) experiments included imaging in the secondary electron, (transmitted) bright field, and high-angle annular dark-field modes while operating in the low kV regime. The results showed that NbS₃-IV samples transform dramatically from smooth nanoribbons into highly textured configurations featuring polyhedral divots and steps. Similar in situ heating experiments conducted with aberration-corrected STEM revealed that bilayers of NbS₃-IV chains convert topotactically into aligned 2*H*-NbS₂ sheets upon loss of sulfur. Atomic resolution imaging, fast Fourier transform analysis, and electron energy loss spectroscopy confirmed these chemical changes, from which we propose an atomistic mechanism for the NbS₃-IV \rightarrow 2*H*-NbS₂ conversion.



■ INTRODUCTION

Recent work has revealed that quasi-1D transition-metal trichalcogenide nanomaterials can exhibit outstanding properties, such as charge density waves, the ability to support high current densities before breakdown, low levels of electronic noise, and anisotropic optical characteristics, 1-5 which make them excellent candidates for next-generation device applications. Niobium trisulfide, NbS3, is an especially interesting system because its polymorphism stands out among transitionmetal trichalcogenides, with up to five NbS3 crystal structures verified to date.⁶⁻⁹ All contain 1D chains of stacked, niobium hexasulfide trigonal prisms assembled into bilayer sheets through interchain Nb···S and S···S interactions. The polymorphs differ in (i) the degree of metal bonding along the chains, that is, the presence or absence of niobium pairing (structural Peierls distortion), and (ii) the repeating pattern and alignment of the bilayer sheets interacting through van der Waals forces. NbS₃-IV, the subject of the present study, exhibits chains oriented along the a-axis that contain niobium pairing and are arranged into repeating sets of bilayers (Figure 1).

Although the structural differences among NbS $_3$ polymorphs are relatively small, they contribute to diverse electronic properties. Transport measurements and/or calculations indicate that NbS $_3$ -I and -IV are semiconducting whereas NbS $_3$ -II and -V are metallic, with NbS $_3$ -II experimentally exhibiting several charge density wave transitions. $^{9-11}$ As pointed out by Canadell and co-workers, "the extra electron provided by the transition metal atom in group V

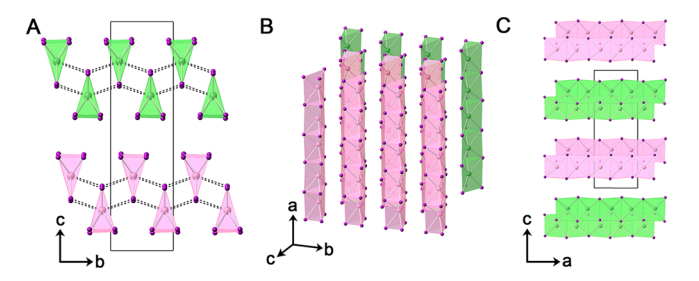


Figure 1. Crystal structure of NbS_3 -IV. Panel (A) shows the view down the chains (down the *a*-axis). Alternating bilayers are colored green and pink, with the van der Waals gap located between them. Dashed lines indicate interchain interactions. The unit cell is outlined in black. Panel (B) shows an angled perspective view that highlights the stacked trigonal prismatic units that comprise each NbS_3 chain. The view down the *b*-axis (panel C) reveals the parallel chains oriented along the *a*-axis.

trichalcogenides may be used to induce either (i) metal-metal bonding (*i.e.* commensurate or incommensurate CDW or Peierls distortions) or (ii) S–S bond reduction."

Received: October 4, 2021 Revised: December 6, 2021 Published: December 21, 2021





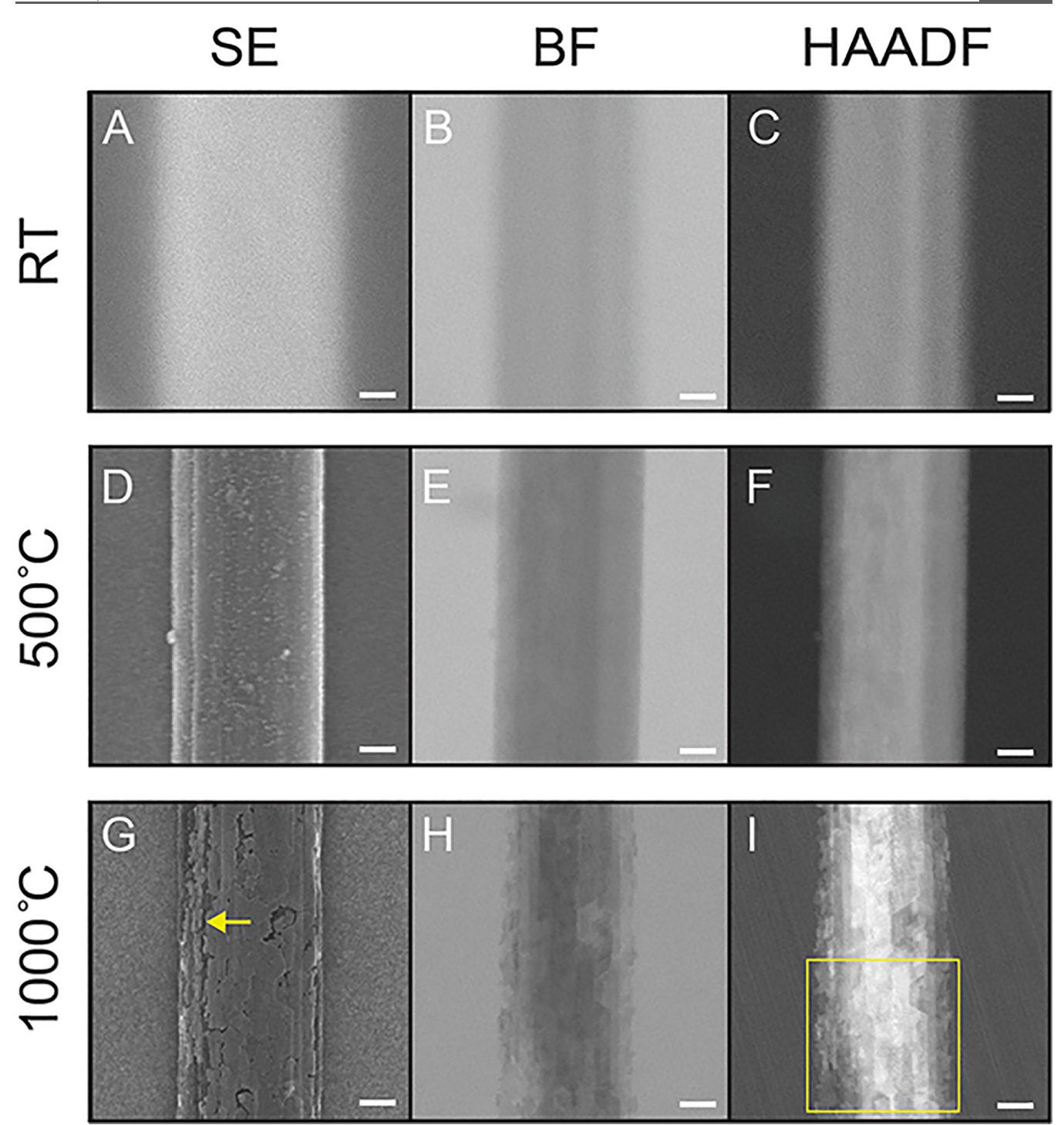


Figure 2. Low kV analysis of a NbS₃-IV nanoribbon at increasing temperatures. This representative sample was imaged using SE, BF, and HAADF modes with a Hitachi SU9000EA microscope. The initial NbS₃-IV nanoribbon at RT (panels A–C) exhibits structural changes by 500 °C (panels D–F), which are especially visible in BF and HAADF modes. By 1000 °C, all images reveal extensive material reconstruction (panels G–I), although the overall nanoribbon morphology is retained. The yellow boxes in panels (G–I) and arrow in (G) correspond to details shown in Figure 3. Scale bars equal 50 nm.

Like other transition-metal trichalcogenides, NbS₃ can be nanostructured by exfoliation, that is, mechanical and chemical methods that cleave the quasi-1D structure along the van der Waals gap, yielding nanoribbons and nanowires suitable for device fabrication. As an example, one recent report described a polarization photodetection device based on mechanically exfoliated NbS₃-I.¹²

Understanding a nanomaterial's chemical and structural features is essential for successful device processing and high-performance applications. Important factors include (i) the details of nanoscale topography, especially at critical interfaces, (ii) the presence and concentration of defects (atomic substitutions, vacancies, disorder at grain boundaries, and reactive dangling bonds), and (iii) the identity, distribution, and evolution of phases with respect to temperature, time,

irradiation, and other conditions relevant to material processing and device performance.

The results described in this contribution illuminate some of these factors with respect to NbS3-IV nanoribbons. Specifically, we use in situ electron microscopy imaging and analysis to observe the dynamics of NbS3-IV nanoribbons at temperatures between room temperature (RT) and 1000 °C. In situ electron microscopy provides excellent tools with which to observe morphological and atomic changes. Such studies of MoS₂ nanomaterials under ultrahigh vacuum conditions have helped establish detailed mechanisms for transformations that occur upon heating. 13-15 To date, however, there has been a single study of metal trichalcogenide dynamics at the nanoscale: a 1987 report by Danot and co-workers describing electron diffraction of NbS₃-I between RT and 500 °C. ¹⁶ These authors concluded that NbS3-I converts to Nb1.2S2, a 3R-type polymorph of NbS2 containing excess intercalated Nb, upon heating at 500 °C for 20 h.

Our study of NbS₃-IV nanoribbons is based on a unique combination of two scanning transmission electron microscopes, each with distinctive capabilities that enable complementary imaging and analysis modalities—secondary electron (SE) imaging, bright field (BF) imaging, high-angle annular dark-field (HAADF) imaging, and electron energy loss spectroscopy (EELS)—while conducting in situ heating experiments. The first of these microscopes, a low kV scanning transmission electron microscope, allows us to monitor changes in internal and surface morphology as NbS₃-IV nanoribbons change with increasing temperature. The second microscope, an aberration-corrected scanning transmission electron microscope with high-resolution EELS, provides atomic and chemical information under similar conditions. By integrating the resulting data sets, we are able to construct a comprehensive picture of the chemical and structural changes occurring during the thermal breakdown of NbS₃-IV nanoribbons, which we present here.

RESULTS AND DISCUSSION

Solvent-exfoliated NbS₃-IV samples with nanoribbon morphology were used for the *in situ* experiments. These nanoribbons are long and narrow (aspect ratio \gg 10). As illustrated in Figure S1, the highly uniform image contrast in all three imaging modes indicates a highly homogenous sample with respect to composition and texture. Dispersions of NbS₃-IV nanoribbons were transferred onto microelectromechanical system (MEMS) chips that interface with heating stages in each microscope for temperature regulation during data collection.

Advantageously, using low kV scanning transmission electron microscopy (STEM) allows for simultaneous imaging of both the sample exterior with the SE detector and internal structural features with BF and HAADF detectors. Figure 2 shows the major morphological changes visible by these imaging modes while heating NbS $_3$ -IV nanoribbons at a rate of five degrees per second. Figure 2 includes highlights at RT, 500, and 1000 °C; the Supporting Information includes data recorded at 100 °C increments.

At RT (Figure 2A–C), we see a single, \sim 200 nm wide NbS₃-IV nanoribbon; the BF and HAADF images indicate a smaller width of \sim 170 nm, which is consistent with the presence of an organic overlayer visible in SE mode (Figure 2A–C). The vertical striations in panels (B) and (C) are consistent with the quasi-1D structure of NbS₃-IV, which leads

to cleavage features along the material's chains (a-axis). Prior atomic force microscopy studies have shown these parallel stripes correspond to bundles or plateaus of metal trichalcogenide chains.²¹

As the sample is heated, the overlayer dissipates by 200 °C, revealing a relatively smooth surface (Supporting Information Figure S2). Once the sample reaches 500 °C, we begin to see new features on the wire surface in the SE imaging mode (Figure 2D) in conjunction with changes in contrast by BF and HAADF (Figure 2E,F). The mottled appearance of the nanoribbon (Figure 2F) corresponds to structural deformations caused by regions gaining or losing atomic density. In all three imaging modes, a certain amount of ribbing along the *a*-axis is visible.

As heating progresses past 500 °C, the darker/denser areas expand across the entire nanoribbon and develop into angular grains (Supporting Information Figure S2). By 1000 °C, the sample is fully reconstructed, although the overall nanoribbon morphology is preserved (Figure 2G–I). SE imaging reveals that the material's surface has become highly textured with hexagonal and trapezoidal plateaus and divots. Interestingly, delamination along the nanoribbon has caused some edge sections to become detached (Figure 2G, arrow). BF and HAADF imaging also reveal polyhedral grains through and along the nanoribbon (Figure 2H,I). The overall width has been reduced to ~152 nm, indicating that material consolidation has occurred.

The structural changes become clearer at higher magnification (Figure 3). The SE image shows layered, polyhedral







Figure 3. Higher magnification views of a niobium sulfide sample at $1000\,^{\circ}\mathrm{C}$ (yellow-boxed area from Figure 2G–I). The yellow arrow in the SE image (A) indicates an area of delamination, and plentiful hexagonal grains are visible across the sample's surface. BF (B) and HAADF (C) images reveal long vertical grains (planks) throughout the sample. The blue arrow points toward a sub-10 nm particle on the sample's surface. Scale bars equal 20 nm.

features on top of larger flat areas. This topography includes numerous cracks and complex edge structures (Figure 3A). BF imaging reveals sub-10 nm particles along the nanoribbon's perimeter, as well as larger trapezoidal features (Figure 3B). Furthermore, there appear to be long, vertical grains or "planks" in the structure that correlate to areas that the stepped polyhedral regions were growing on. HAADF imaging highlights the consolidation of material toward the nanoribbon's core, as indicated by its brightness compared to the thinner periphery (Figure 3C). Also, as in the case of the SE image, the HAADF images exhibit what appears to be a horizontal alignment in the newly formed polyhedral steps.

To clarify the atomic basis of these changes, similar *in situ* heating experiments were conducted using an Nion Ultra-STEM 100 microscope to collect atomic resolution HAADF images and EELS data. As shown in Figure 4A, a NbS₃-IV nanoribbon at RT presents well-resolved, parallel niobium sulfide chains with an experimental spacing of 0.526 nm, which compares favorably to a theoretical value of 0.497 nm, as well

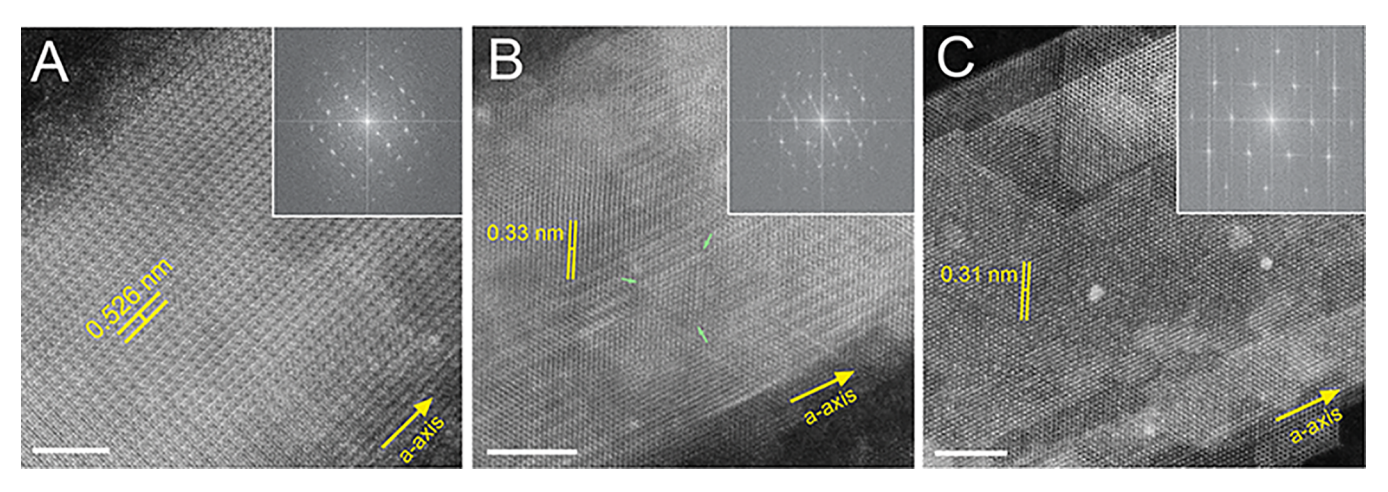


Figure 4. Atomic resolution STEM imaging (Nion UltraSTEM 100) of a niobium sulfide nanoribbon at increasing temperatures. (A) RT image and FFT (inset) are consistent with the starting material, NbS₃-IV. (B) Image at 500 °C; the existence of triangular grains (greens arrows at the vertex points) and a more complex FFT (inset) indicate the presence of mixed phases. (C) Data at 1000 °C are consistent with polyhedral grains of NbS₂. All FFTs correspond to the entire ribbon region shown in the panel. Scale bars equal 5 nm.

as a distinct orthogonal pattern due to niobium—niobium pairing along these chains; the atomic details of this feature can be clearly seen by high-resolution transmission electron microscopy (HR-TEM, Supporting Information Figure S3). The fast Fourier transform (FFT) of the atomic resolution image was indexed to the [001] zone axis of NbS₃-IV using d_{100} and d_{010} measurements of 0.679 and 0.492 nm, respectively, which are in close agreement with the calculated values of 0.675 and 0.497 nm from the crystal structure (Figure 4A inset).

Upon reaching 500 °C, many differences immediately become visible (Figure 4B). One striking change is the appearance of bright lines at 60 and 120° with respect to the original NbS3 chains, with some of them outlining triangular grains (Figure 4B, green arrows). The formation of such triangular crystals is a distinctive feature of many transitionmetal dichalcogenide systems, including NbS₂. ²²⁻²⁴ Although NbS3-IV chains are present, new atomic rows in various orientations indicate that a structural transformation is underway. For example, the most prevalent spacing between the newly formed rows is 0.33 nm, smaller than that \sim 0.5 nm seen for NbS₃. The FFT contains several identifiable patterns including the original RT pattern of NbS3-IV, a new diamondshaped configuration, and a nascent ring (Figures 4B inset and S4). Furthermore, the FFTs from 5 nm domains of this nanoribbon at 500 °C exhibit a variety of patterns and orientations consistent with polycrystallinity (Figure S5).

Imaging at 1000 °C reveals a completely altered atomic structure (Figure 4C) compared to the starting material (Figure 4A). The quasi-1D chains have been replaced by horizontally stepped layers with polyhedral islands and a hexagonal atomic structure. FFT analysis provides d-spacing values of 0.302, 0.301, and 0.175 nm, consistent with the (010), (100), and (110) lattice planes of NbS₂, respectively, oriented along the [001] zone axis (Figure 4C). Although these values are most consistent with the 1T phase of NbS₂ (Table S1),²⁵ several factors mitigate this assignment: (i) trigonal prismatic coordination is strongly favored in the NbS₂ system, that is, the 2H and 3R polymorphs are almost always isolated, and 2H is considered the thermodynamically stable phase;²⁶ there have been only a few reports of NbS₂ containing octahedral niobium (1T-NbS₂) as monolayers or thin film

samples; ^{27,28} (ii) it is often not straightforward to unambiguously distinguish these polymorphs by diffraction, especially in this sample orientation; ²⁹ and (iii) 3*R*-NbS₂ usually forms from the elements under stoichiometric or sulfur-deficient conditions. ^{29,30} These factors lead us to believe that the niobium sulfide phase formed in our *in situ* experiments at 1000 °C is likely 2*H*-NbS₂, pending future confirmation by *in situ* temperature-dependent Raman spectroscopy.

Figure 5 presents high-resolution dark-field STEM images of the same nanoribbon at 1000 °C. In Figure 5A, imaging shows

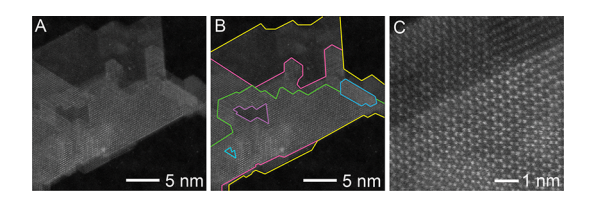


Figure 5. Atomic-scale dark-field imaging (Nion UltraSTEM 100) of a niobium sulfide nanoribbon at 1000 °C. Panels (A) and (B) show that the nanoribbon is now composed of layered grains; six distinct regions with varying thicknesses are outlined in different colors. Panel (C) shows a higher magnification view of the hexagonal atomic structure.

that the end of the nanoribbon is composed of regions of varying thickness, which can be distinguished by their relative contrast in HAADF mode. Each of these layers is outlined with a different color in panel 5B. The layers adopt irregular shapes composed of intergrown triangles and hexagons, and additional smaller islands (blue outline) and divots (purple outline) can be identified. All grain boundaries are atomically sharp. The well-resolved hexagonal lattice (Figure 5C) is characteristic of monolayer transition-metal dichalcogenides as well as multilayer 2H-phases like 2H-MoS₂ and 2H-TaS₂.³¹ The fine atomic structure is also visualized, most notably seen by the bright niobium atoms in the hexagonal atomic arrangement with bond distances of 0.21 nm between neighboring atoms and 0.46 nm across the hexagon (Figure 5C). Moreover, in this image, there is a step in thickness from one layer to another as evidenced by the contrast drop in the hexagonal shape of the atomic layers continuing across the variation in height. In

addition, the region encompassed by panel (C) appears free of vacancies or other defects.

During our work with NbS₃ polymorphs, we have noted numerous instances of chain twisting visible by high-resolution electron microscopy. One example is shown in Figure 6A: this

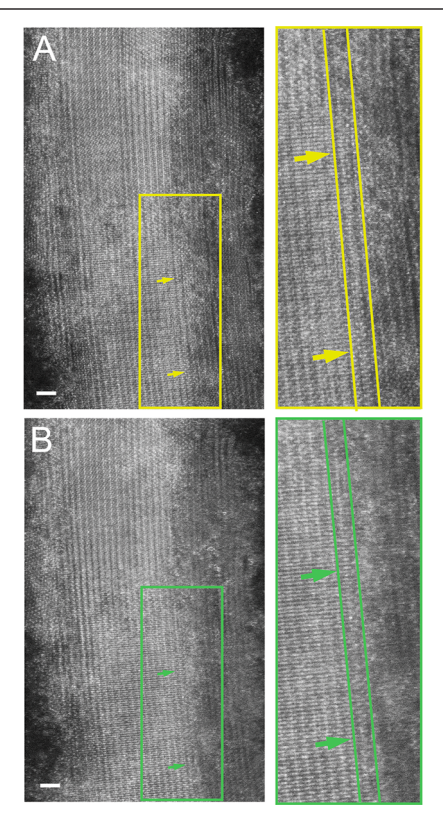


Figure 6. Atomic resolution STEM imaging (Nion UltraSTEM 100) of a NbS₃-IV nanoribbon that reveals the twisting and untwisting of an individual NbS₃ chain. (A) As-prepared sample at RT. The yellow box highlights an area containing a single twisted NbS₃ chain. In the magnified view in the right, this chain is located between the parallel yellow lines; arrows indicate the length of this chain's 60° twist. (B) Sample heated to 100 °C where only straight NbS₃-IV chains are visible in this image. All scale bars equal 1 nm.

NbS3-IV nanoribbon at RT contains a twisted NbS3 chain (between parallel yellow lines within the yellow box). The 60° twist that is visible spans 6-7 nm, as indicated by the arrows. Perhaps importantly, this chain is located near the nanoribbon edge where it likely experiences less stabilization through interchain interactions with fewer neighboring chains than interior chains. Upon heating to 100 °C, this particular chain appears disordered (located between parallel green lines in Figure 6B) and may be in a transitional state from twisted to untwisted. Furthermore, FFT analysis shows a well-defined NbS₃ pattern (straight chain) versus a smeared pattern (twisted chain) at RT, as well as a well-defined NbS₃ pattern at 100 °C that corresponds to the now untwisted straight chain (Supporting Information Figure S6).32 This observation suggests that annealing, even at such a low temperature, can allow twisted chains to relax into a more stable, straight alignment. Further investigations are needed to identify the prevalence of chain twisting in NbS₃ samples and the impact of this novel defect on electronic properties, including charge density wave behavior.

Recent reports by Zettl and co-workers described metal trichalcogenide chains encapsulated within carbon or boron nitride nanotubes; in particular, single-, double-, and triple-chain NbSe₃ adopts spiraling (helical torsional wave) morphologies with a wavelength for 2π rotation of 41 nm. This value (6.8 nm for 60° rotation) is comparable to what we observe here for NbS₃-IV. Although these encapsulation studies suggest that nanoconfinement is required to stabilize twisted metal trichalcogenide chains, here, we see that twisted NbS₃ chains may be present within the crystalline lattice.

EELS provides additional insight about the chemical transformations taking place during in situ heating. Figure 7

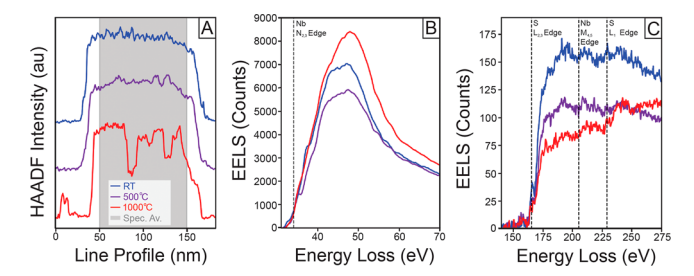


Figure 7. EELS analysis of a NbS $_3$ -IV nanoribbon at RT, 500, and 1000 °C. Panel (A) displays the HAADF intensity over the width of a representative nanoribbon; EELS spectra in panels (B) and (C) were collected from the region highlighted in gray. Panel (B) shows the Nb edges of the EELS spectra between 30 and 70 eV and panel (C) shows the fine structure of S and Nb signals after background subtraction in the region of 150–275 eV.

summarizes the HAADF intensities and EELS spectra taken across the main body of the nanoribbon sample at RT, 500, and 1000 °C, Supporting Information Figure S7 displays the zones imaged on the nanoribbons from which the EELS spectra were collected. In Figure 7A, the HAADF intensity profiles reflect morphology changes related to the nanoribbon thinning across its width, that is, consolidating toward the ribbons' core, as well as the stepped nature of the newly formed grains. The shaded region within Figure 7A corresponds to the area analyzed by EELS, the specific spectra of which are seen in panels 7B,C. By specifically investigating the higher energy signals (60-70 eV for Nb and 250-275 eV for S), we can see that the Nb intensity remains relatively constant between RT and 500 °C while the S intensity decreases significantly, with this trend continuing from 500 to 1000 °C (Figure 7B,C). This is strongly indicative of S loss from the nanoribbon as the chemical composition changes from NbS₃ to NbS₂, which results in a higher relative amount of Nb per unit thickness. Moreover, the large difference seen in the S peak range comes from a higher M4,5 cross-section, consistent with a change in the S bonding environment (Figure 7C).

It is critical to note that, especially at high temperature, the high-energy electrons of the STEM probe will selectively knock out S atoms as a form of beam damage. However, by comparing the EELS data between 500 and 1000 °C, we observe a clear change in the fine structure of the Nb N-edge and the S L-edge indicating a fundamental change in bonding and not just a removal of material, which is consistent with the imaging analysis. Furthermore, heating-enhanced beam damage would still be present at 500 °C, and this spectrum does not exhibit a significant change in the relative concentration of

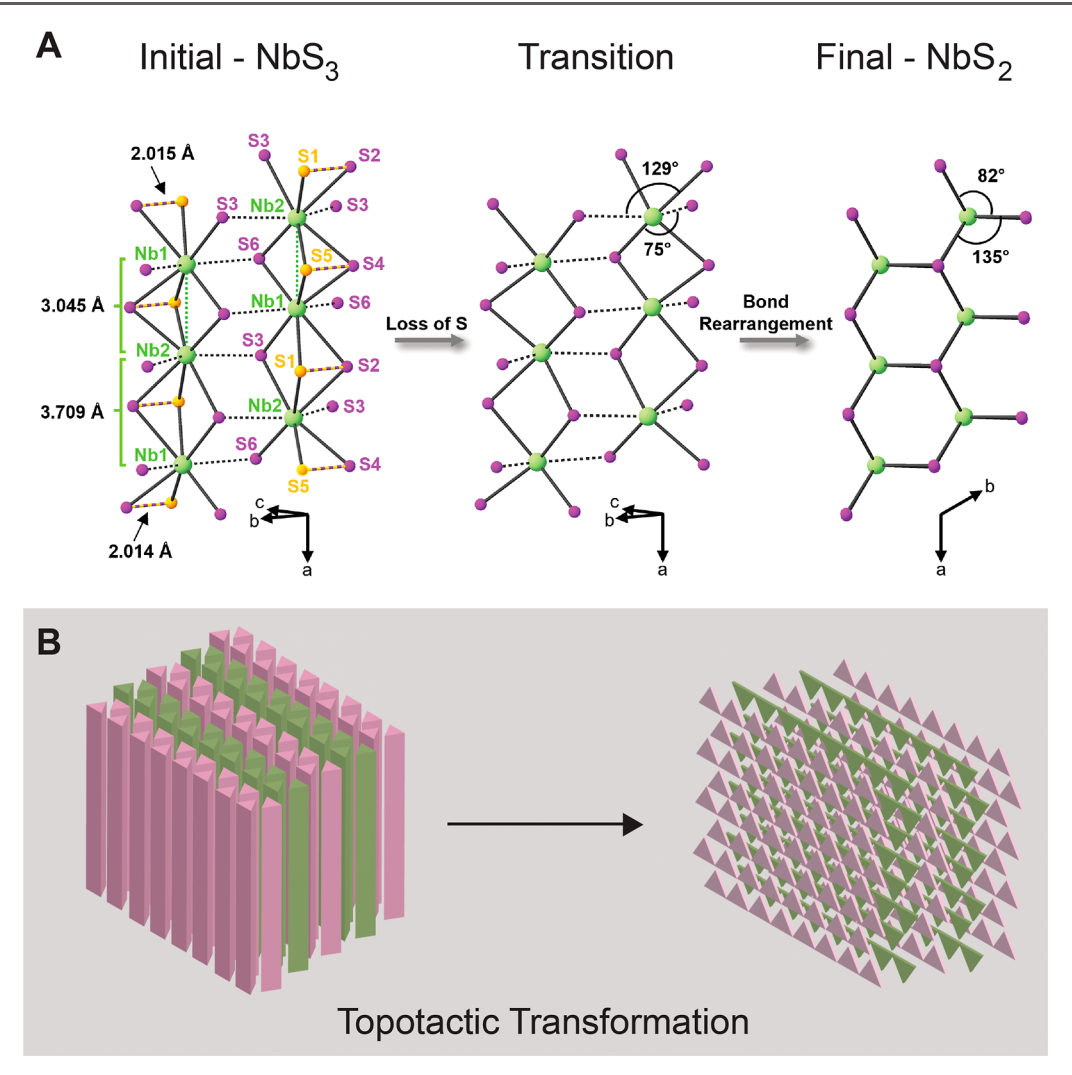


Figure 8. Panel (A): proposed mechanism of structural and compositional changes in NbS₃-IV nanoribbons upon heating from RT to 1000 °C. This sequence of structures shows the loss of sulfur and additional atomic movements required to transform NbS₃-IV into NbS₂. Panel (B): schematic of overall structural and compositional changes in NbS₃-IV nanoribbons upon heating from RT to 1000 °C, which highlights the topotactic nature of the NbS₃-IV \rightarrow NbS₂ transformation.

Nb and S. Instead, we observe both cross-sections reduce by a similar amount between RT and 500 $^{\circ}$ C. Thus, EELS confirms that the nanowire has fully transitioned to NbS₂ at 1000 $^{\circ}$ C.

Based on these data, we present a mechanism for the changes that occur when NbS₃-IV nanoribbons are heated. As shown in detail by Figure 8A, the structure of NbS3-IV is based on stacked trigonal prismatic niobium hexasulfide units, within which the bonding can be described as $Nb^{4+}(S_2)^{2-}S^{2-}$. Every other pair of stacked niobium hexasulfide units contains Nb-Nb bonding, that is, Nb1-Nb2 pairs at a distance of 3.045 Å. In addition, Nb···S interchain interactions define chain bilayers into 2D sheets. It seems most likely that the sulfur released upon heating corresponds to one atom from each $(S_2)^{2-}$, that is, (S1, S2)2- or (S4, S5)2-, which are less strongly bound to niobium than the S2- coordinated between niobium centers across the van der Waals gap, that is, S3 or S6. One sulfur from each of these $(S_2)^{2-}$ is labeled in yellow (Figure 8A). Upon loss of this sulfur by 500 °C, relatively small atomic movements are needed to facilitate bond formation between each niobium and two additional sulfur atoms from adjacent chains, which is aided by the pre-existing Nb···S interactions. This results in half of a new niobium hexasulfide polyhedron,

the building block of NbS₂. Furthermore, sulfur loss from the NbS₃ structure causes the resulting NbS₂ nanoribbon to have greater atomic density and a reduced diameter across its width. As these chemical changes proceed, the niobium sulfides fuse to form continuous NbS₂ sheets of edge-sharing niobium hexasulfide polyhedra (Figure 8). These structural changes are reflected in the complex FFT at 500 °C (Figure 4B). In addition, the observed cracking (Figure 3) is consistent with the significant increase in material density, from 4.126 g cm⁻³ for NbS₃-IV to 4.4 g cm⁻³ for NbS₂.^{7,25} The formation of NbS₂ is complete by 1000 °C and accompanied by nanoscale reconstruction into complex layered grains (Figures 3-5). Although the niobium hexasulfide polyhedra could adopt trigonal prismatic geometry (consistent with the 2H and 3R polymorphs of NbS₂) or octahedral geometry (consistent with the 1T polymorph of NbS₂), our preliminary conclusion is that this product is most likely 2H-NbS₂.

Because the overall NbS_3 -IV \rightarrow NbS_2 reaction involves a NbS_3 -IV chain bilayer transforming into a NbS_2 monolayer, an important feature of this mechanism is its topotactic nature, which preserves the location of the van der Waals gap within the two lattices (Figure 8B). The final NbS_2 product maintains

the overall morphology of the starting NbS₃ nanoribbon, with minor alterations due to material migration and nanostructuring effects. The sequence illustrated in Figure 8A contrasts with a proposed mechanism of ZrS_xSe_{2-x} oxidation, which invokes collapse of the van der Waals gap through the formation of interlayer Zr–S and Zr–O bonds.

The NbS₃-I \rightarrow Nb_{1,2}S₂ transformation mechanism proposed by Danot and co-workers entails a similar rearrangement to the one in Figure 8, which is not surprising due to the structural similarities between NbS₃-I and NbS₃-IV. However, they conclude that Nb_{1,2}S₂ rather than stoichiometric NbS₂ forms under their experimental conditions. Certainly, Nb_{1,2}S₂ is a known phase, but no definitive evidence for Nb_{1,2}S₂ versus NbS₂ was provided by Danot and co-workers. Furthermore, according to ex situ studies, heating NbS₃-I at 800 °C for 1.5 h leads to 2*H*-NbS₂. We also do not find evidence of Nb_{1,2}S₂, although our samples are not in the optimal orientation to detect Nb intercalation. Mechanisms similar to that summarized in Figure 8 have been used by several research groups to explain the introduction of sulfur vacancies in TiS₃ and ZrS₃. 37,38

CONCLUSIONS

In summary, a combination of in situ imaging and spectroscopy analysis tools have allowed us to construct a comprehensive picture of the structural changes experienced by NbS3-IV nanoribbons during thermal treatment. Low kV imaging with in situ heating revealed that the nanoribbon's originally smooth surface changes to one with a highly textured morphology composed of polyhedral divots and plateaus throughout the structure. UltraSTEM imaging with in situ heating illuminated the transformation of aligned NbS3-IV chains into NbS2 with complex layered morphologies. We also observed how moderate heating prompts the relaxation of NbS3-IV defects, specifically chain twisting, to improve interchain alignment. The correlated FFT and EELS data provided important information about the chemical changes taking place during the NbS₃-IV \rightarrow NbS₂ transformation, leading to a likely mechanism. Although chalcogen loss upon heating is generally well established for transition-metal chalcogenides, the structural specifics of the NbS₃ system and the in situ experiments reported here allow us to propose a detailed atomistic mechanism for sulfur loss and subsequent rearrangements.

We anticipate that further insights will emerge from correlating the results of this study with macroscopic techniques, such as temperature-dependent and angle-resolved Raman spectroscopy (under UHV and/or inert atmosphere conditions) and neutron scattering. These techniques can provide potentially more detailed information about the alignment of NbS₃ chains and NbS₂ polytypes.

The results of this study will aid the preparation and processing of nanostructured NbS₃ for device incorporation. ^{5,12,39} Intriguingly, these dynamics reflect the conversion of a quasi-1D quantum material, NbS₃, into a 2D quantum material, NbS₂, which is an area of significant interest as the development of low dimensional materials for quantum technologies accelerates. The integration of low kV imaging, UltraSTEM imaging, and EELS analysis provides an ideal platform for such studies.

EXPERIMENTAL DETAILS

Preparation of NbS₃-IV Crystals. Niobium powder (99.99%) was purchased from Sigma-Aldrich, sulfur powder (>99.9%) from J.T. Baker, and bromine (>99%) from ACROS Organics. A stoichiometric mixture of 1.4753 g (15.9 mmol) of niobium and 1.5647 g (48.8 mmol) of sulfur was ground gently using an agate mortar and pestle. Next, 10.0 μ L of liquid bromine (2.1 mg cm⁻³ for a ~15 cm³ volume ampule) was micropipetted into a quartz glass ampule (10 mm ID, 14 mm OD, 170 mm length) suspended in an acetonitrile/dry ice bath, followed by the addition of the ground powder mixture. The ampule was evacuated and backfilled with Ar three times before being vacuum-sealed (10^{-2} Torr) and placed in a three-zone furnace. The reaction was heated at a rate of 5 °C min⁻¹ to 670-570 °C (source zone-growth zone) for 10 d. After heating was complete, the ampule was left in the furnace to cool naturally to RT. The resulting dark gray fibers of NbS3-IV were collected and placed in a vacuum oven at RT for 30 min to remove residual bromine.

Exfoliation of NbS₃-IV Crystals into Nanoribbons. 4.7 mg of NbS₃-IV crystals was added to \sim 12 mL of acetone in a 50 mL centrifuge tube. This sample was probe-sonicated at 28 A for 1 h. After sonication, the sample was allowed to sit until larger particles settled (15–30 min). The decanted supernatant containing NbS₃-IV nanoribbons was used for electron microscopy.

Microscopy. *In situ* imaging of NbS₃-IV with a Hitachi SU9000EA low KV STEM instrument was conducted using an accelerating voltage of 30 kV and a current of 10 μ A. Exfoliated NbS₃-IV dispersed in acetone was brushed onto the heating portion of a four-contact Norcada microelectromechanical heating chip, with 2–3 μ m diameter holes. The chip was then placed onto a single tilt Hitachi Blaze heating holder that was then inserted into the microscope. Initial images were taken, and the sample was then heated at a rate of 5 °C s⁻¹ to the respective imaging temperature in 100° increments. All images were collected simultaneously with the SE, BF, and high-angle dark-field detectors.

In situ imaging and analysis with the Nion UltraSTEM 100. Assynthesized NbS $_3$ (iv) nanowires were dispersed in isopropanol and brushed onto the heating portion of a Protochips MEMS chip and heated at a rate of 5 °C s $^{-1}$ to the respective imaging and analysis temperature.

For STEM imaging and EELS, data were acquired in 100 °C increments from RT to 1000 °C. Because the heating process induces a significant drift, the sample stage must be allowed to thermally equilibrate before data collection. This requirement precludes direct observations during temperature ramping.

A Thermo Fisher Titian STEM was also used for non in situ imaging of the NbS₃ nanoribbons.

Data Processing. Images were processed to maximize brightness and contrast in Photoshop. All measurements were conducted in ImageJ.

ASSOCIATED CONTENT

Supporting Information

The Supporting Information is available free of charge at https://pubs.acs.org/doi/10.1021/acs.chemmater.1c03411.

Images of a NbS $_3$ -IV nanoribbon at RT; images collected from RT to 1000 °C in 100 °C increments; HR-TEM image of a NbS $_3$ -IV nanoribbon; breakdown of the FFT for the nanoribbon sample at 500 °C; table of experimental and simulated diffraction FFT measurements; FFTs from specific regions of a nanoribbon sample at 500 °C; FFTs from straight, twisted, and untwisted NbS $_3$ chain regions; and images of the line scan region from which EELS spectra were obtained (PDF)

AUTHOR INFORMATION

Corresponding Authors

- Eric V. Formo Georgia Electron Microscopy, University of Georgia, Athens, Georgia 30602, United States;
- o orcid.org/0000-0002-5604-4884; Email: eformo@uga.edu
- Tina T. Salguero Department of Chemistry, University of Georgia, Athens, Georgia 30602, United States;
- o orcid.org/0000-0001-9396-3583; Email: salguero@uga.edu

Authors

Jordan A. Hachtel — Center for Nanophase Materials Sciences, Oak Ridge National Laboratory, Oak Ridge, Tennessee 37831, United States; orcid.org/0000-0002-9728-0920

Yassamin Ghafouri – Department of Chemistry, University of Georgia, Athens, Georgia 30602, United States

Matthew A. Bloodgood – Department of Chemistry, University of Georgia, Athens, Georgia 30602, United States

Complete contact information is available at: https://pubs.acs.org/10.1021/acs.chemmater.1c03411

Notes

The authors declare no competing financial interest.

ACKNOWLEDGMENTS

A portion of this research was conducted at the Center for Nanophase Materials Sciences, which is a DOE Office of Science User Facility. The Hitachi SU9000EA microscope used in this work was acquired with a Major Research Instrumentation (MRI) award from the U.S. National Science Foundation (award number 1919942).

REFERENCES

- (1) Island, J. O.; Molina-Mendoza, A. J.; Barawi, M.; Biele, R.; Flores, E.; Clamagirand, J. M.; Ares, J. R.; Sánchez, C.; Van Der Zant, H. S. J.; D'Agosta, R.; Ferrer, I. J.; Castellanos-Gomez, A. Electronics and Optoelectronics of Quasi-1D Layered Transition Metal Trichalcogenides. 2D Mater. 2017, 4, 022003.
- (2) Geremew, A. K.; Rumyantsev, S.; Bloodgood, M. A.; Salguero, T. T.; Balandin, A. A. Unique features of the generation-recombination noise in quasi-one-dimensional van der Waals nanoribbons. *Nanoscale* **2018**, *10*, 19749–19756.
- (3) Geremew, A.; Bloodgood, M. A.; Aytan, E.; Woo, B. W. K.; Corber, S. R.; Liu, G.; Bozhilov, K.; Salguero, T. T.; Rumyantsev, S.; Rao, M. P.; Balandin, A. A. Current Carrying Capacity of Quasi-1D ZrTe₃ Van Der Waals Nanoribbons. *IEEE Electron Device Lett.* **2018**, 39, 735–738.
- (4) Patra, A.; Rout, C. S. Anisotropic quasi-one-dimensional layered transition-metal trichalcogenides: synthesis, properties and applications. *RSC Adv.* **2020**, *10*, 36413.
- (5) Wen, X.; Lei, W.; Ni, L.; Yang, L.; Zhang, P.; Liu, Y.; Chang, H.; Zhang, W. Evaluating the Electrical Characteristics of Quasi-One-Dimensional ZrTe₃ Nanoribbon Interconnects. *ACS Appl. Electron. Mater.* **2021**, *3*, 4228–4235.
- (6) Rijnsdorp, J.; Jellinek, F. The crystal structure of niobium trisulfide, NbS₃. *J. Solid State Chem.* **1978**, 25, 325–328.
- (7) Bloodgood, M. A.; Wei, P.; Aytan, E.; Bozhilov, K. N.; Balandin, A. A.; Salguero, T. T. Monoclinic Structures of Niobium Trisulfide. *APL Mater.* **2018**, *6*, 026602.
- (8) Zupanič, E.; van Midden, H. J. P.; van Midden, M. A.; Šturm, S.; Tchernychova, E.; Pokrovskii, V. Y.; Zybtsev, S. G.; Nasretdinova, V. F.; Zaitsev-Zotov, S. V.; Chen, W. T.; Pai, W. W.; Bennett, J. C.; Prodan, A. Basic and charge density wave modulated structures of NbS₃-II. *Phys. Rev. B* **2018**, *98*, 174113.

- (9) Conejeros, S.; Guster, B.; Alemany, P.; Pouget, J.-P.; Canadell, E. Rich Polymorphism of Layered NbS₃. *Chem. Mater.* **2021**, 33, 5449–5463
- (10) Monceau, P. Electronic Crystals: An Experimental Overview. *Adv. Phys.* **2012**, *61*, 325–581.
- (11) Zybtsev, S. G.; Pokrovskii, V. Y.; Nasretdinova, V. F.; Zaitsev-Zotov, S. V.; Pavlovskiy, V. V.; Odobesco, A. B.; Pai, W. W.; Chu, M. W.; Lin, Y. G.; Zupanic, E.; van Midden, H. J. P.; Sturm, S.; Tchernychova, E.; Prodan, A.; Bennett, J. C.; Mukhamedshin, I. R.; Chernysheva, O. V.; Menushenkov, A. P.; Loginov, V. B.; Loginov, B. A.; Titov, A. N.; Abdel-Hafiez, M. NbS₃: A unique quasi one-dimensional conductor with three charge density wave transitions. *Phys. Rev. B* **2017**, *95*, 035110.
- (12) Wang, Y.; Wu, P.; Wang, Z.; Luo, M.; Zhong, F.; Ge, X.; Zhang, K.; Peng, M.; Ye, Y.; Li, Q.; Ge, H.; Ye, J.; He, T.; Chen, Y.; Xu, T.; Yu, C.; Wang, Y.; Hu, Z.; Zhou, X.; Shan, C.; Long, M.; Wang, P.; Zhou, P.; Hu, W. Air-Stable Low-Symmetry Narrow-Bandgap 2D Sulfide Niobium for Polarization Photodetection. *Adv. Mater.* 2020, 32, 2005037.
- (13) Sang, X.; Li, X.; Puretzky, A. A.; Geohegan, D. B.; Xiao, K.; Unocic, R. R. Atomic Insight into Thermolysis-Driven Growth of 2D MoS₂. Adv. Funct. Mater. **2019**, 29, 1902149.
- (14) Fei, L.; Lei, S.; Zhang, W.-B.; Lu, W.; Lin, Z.; Lam, C. H.; Chai, Y.; Wang, Y. Direct TEM observations of growth mechanisms of two-dimensional MoS₂ flakes. *Nat. Commun.* **2016**, *7*, 12206.
- (15) Zink, N.; Therese, H. A.; Pansiot, J.; Yella, A.; Banhart, F.; Tremel, W. *In Situ* Heating TEM Study of Onion-like WS₂ and MoS₂ Nanostructures Obtained via MOCVD. *Chem. Mater.* **2008**, *20*, 65–71
- (16) Kurdi, M.; Marie, A.-M.; Danot, M. The crystallographic mechanism of the NbS_3 to $Nb_{1.12}S_2$ transition. *Solid State Commun.* **1987**, *64*, 395–399.
- (17) Schürmann, U.; Winkler, M.; König, J. D.; Liu, X.; Duppel, V.; Bensch, W.; Böttner, H.; Kienle, L. *In Situ* TEM Investigations on Thermoelectric Bi₂Te₃/Sb₂Te₃ Multilayers. *Adv. Eng. Mater.* **2012**, *14*, 139–143.
- (18) Liu, C.; Malladi, S. K.; Xu, Q.; Chen, J.; Tichelaar, F. D.; Zhuge, X.; Zandbergen, H. W. In-situ STEM imaging of growth and phase change of individual CuAlX precipitates in Al alloy. *Sci. Rep.* **2017**, *7*, 2184.
- (19) Liu, X.; Wood, J. D.; Chen, K.-S.; Cho, E.; Hersam, M. C. *In Situ* Thermal Decomposition of Exfoliated Two-Dimensional Black Phosphorus. *J. Phys. Chem. Lett.* **2015**, *6*, 773–778.
- (20) Xu, F.-F.; Ebina, Y.; Bando, Y.; Sasaki, T. *In Situ* Transmission Electron Microscopic Study of Perovskite-Type Niobate Nanosheets under Electron-Irradiation and Heating. *J. Phys. Chem. B* **2003**, *107*, 66698–666703.
- (21) Lipatov, A.; Loes, M. J.; Lu, H.; Dai, J.; Patoka, P.; Vorobeva, N. S.; Muratov, D. S.; Ulrich, G.; Kästner, B.; Hoehl, A.; Ulm, G.; Zeng, X. C.; Rühl, E.; Gruverman, A.; Dowben, P. A.; Sinitskii, A. Quasi-1D TiS₃ Nanoribbons: Mechanical Exfoliation and Thickness-Dependent Raman Spectroscopy. *ACS Nano* **2018**, *12*, 12713–12720.
- (22) Tang, L.; Tan, J.; Nong, H.; Liu, B.; Cheng, H.-M. Chemical Vapor Deposition Growth of Two-Dimensional Compound Materials: Controllability, Material Quality, and Growth Mechanism. *Acc. Mater. Res.* **2021**, *2*, 36–47.
- (23) Ge, W.; Kawahara, K.; Tsuji, M.; Ago, H. Large-scale synthesis of NbS₂ nanosheets with controlled orientation on graphene by ambient pressure CVD. *Nanoscale* **2013**, *5*, 5773–5778.
- (24) Zhao, S.; Hotta, T.; Koretsune, T.; Watanabe, K.; Taniguchi, T.; Sugawara, K.; Takahashi, T.; Shinohara, H.; Kitaura, R. Two-dimensional metallic NbS₂: growth, optical identification and transport properties. 2D Mater. **2016**, 3, 025027.
- (25) Jellinek, F.; Brauer, G.; Müller, H. Molybdenum and Niobium Sulphides. *Nature* **1960**, *185*, 376–377.
- (26) Ravnik, J.; Vaskivskyi, I.; Gerasimenko, Y.; Diego, M.; Vodeb, J.; Kabanov, V.; Mihailovic, D. D. Strain-Induced Metastable Topological Networks in Laser-Fabricated TaS₂ Polytype Hetero-

structures for Nanoscale Devices. ACS Appl. Nano Mater. 2019, 2, 3743-3751.

- (27) Carmalt, C. J.; Manning, T. D.; Parkin, I. P.; Peters, E. S.; Hector, A. L. Formation of a new (1T) trigonal NbS₂ polytype via atmospheric pressure chemical vapor deposition. *J. Mater. Chem.* **2004**, *14*, 290–291.
- (28) Leroux, M.; Cario, L.; Bosak, A.; Rodière, P. Traces of charge density waves in NbS₂. *Phys. Rev. B* **2018**, *97*, 195140.
- (29) Witteveen, C.; Górnicka, K.; Chang, J.; Månsson, M.; Klimczuk, T.; von Rohr, F. O. Polytypism and superconductivity in the NbS2 system. *Dalton Trans.* **2021**, *50*, 3216–3223.
- (30) Fisher, W. G.; Sienko, M. J. Stoichiometry, structure, and physical properties of niobium disulfide. *Inorg. Chem.* **1980**, *19*, 39–43.
- (31) Eda, G.; Fujita, T.; Yamaguchi, H.; Voiry, D.; Chen, M.; Chhowalla, M. Coherent Atomic and Electronic Heterostructures of Single-Layer MoS₂. ACS Nano **2012**, *6*, 7311–7317.
- (32) Gailhanou, M.; Roussel, J. M. Diffraction from twisted nanowires: helicity revealed by anisotropy. *J. Appl. Crystallogr.* **2018**, *51*, 1586–1596.
- (33) Pham, T.; Oh, S.; Stetz, P.; Onishi, S.; Kisielowski, C.; Cohen, M. L.; Zettl, A. Torsional instability in the single-chain limit of a transition metal trichalcogenide. *Science* **2018**, *361*, 263–266.
- (34) Stonemeyer, S.; Cain, J. D.; Oh, S.; Azizi, A.; Elasha, M.; Thiel, M.; Song, C.; Ercius, P.; Cohen, M. L.; Zettl, A. Stabilization of NbTe₃, VTe₃, and TiTe₃ via Nanotube Encapsulation. *J. Am. Chem. Soc.* **2021**, *143*, 4363–4568.
- (35) Jo, S. S.; Singh, A.; Yang, L.; Tiwari, S. C.; Hong, S.; Krishnamoorthy, A.; Sales, M. G.; Oliver, S. M.; Fox, J.; Cavalero, R. L.; Snyder, D. W.; Vora, P. M.; McDonnell, S. J.; Vashishta, P.; Kalia, R. K.; Nakano, A.; Jaramillo, R. Growth Kinetics and Atomistic Mechanisms of Native Oxidation of ZrS_xSe_{2-x} and MoS₂ Crystals. *Nano Lett.* **2020**, *20*, 8592–8599.
- (36) Tao, Y.; Gao, Q.; Wang, X.; Wu, X.; Mao, C.; Zhu, J. NbN and NbS2 Nanobelt Arrays: In-Situ Conversion Preparation and Field-Emission Performance. J. Nanosci. Nanotechnol. 2011, 11, 3345—3349.
- (37) Tian, Z.; Han, C.; Zhao, Y.; Dai, W.; Lian, X.; Wang, Y.; Zheng, Y.; Shi, Y.; Pan, X.; Huang, Z.; Li, H.; Chen, W. Efficient photocatalytic hydrogen peroxide generation coupled with selective benzylamine oxidation over defective ZrS3 nanobelts. *Nat. Commun.* **2021**, *12*, 2039.
- (38) Tian, Z.; Guo, X.; Wang, D.; Sun, D.; Zhang, S.; Bu, K.; Zhao, W.; Huang, F. Enhanced Charge Carrier Lifetime of TiS₃ Photoanode by Introduction of S₂²⁻ Vacancies for Efficient Photoelectrochemical Hydrogen Evolution. *Adv. Funct. Mater.* **2020**, *30*, 2001286.
- (39) Wu, W.; Wang, Y.; Niu, Y.; Wang, P.; Chen, M.; Sun, J.; Wang, N.; Wu, D.; Zhao, Z. Thermal Localization Enhanced Fast Photothermoelectric Response in a Quasi-One-Dimensional Flexible NbS3 Photodetector. ACS Appl. Mater. Interfaces 2020, 12, 14165—14173.

□ Recommended by ACS

CVD Growth of a Horizontally Aligned One-Dimensional Van der Waals Material, Nb₂Se₉

Sang Hoon Lee, Jae-Young Choi, et al.

JANUARY 11, 2023

CRYSTAL GROWTH & DESIGN

READ 🗹

Anionic Flow Valve Across Oxide Heterointerfaces by Remote Electron Doping

Yunkyu Park, Junwoo Son, et al.

NOVEMBER 17, 2022

NANO LETTERS

READ 🗹

Crystallization Behavior of Zinc-Doped Nb₂O₅ Thin Films Synthesized by Atomic Layer Deposition

Alexander C. Kozen, Zachary R. Robinson, et al.

AUGUST 11, 2022

ACS APPLIED ELECTRONIC MATERIALS

READ 🗹

Synthesis of a Selectively Nb-Doped WS₂-MoS₂ Lateral Heterostructure for a High-Detectivity PN Photodiode

Van Tu Vu, Woo Jong Yu, et al.

AUGUST 01, 2022

ACS NANO

READ **C**

Get More Suggestions >